Modelling of Sediment Gravity Flows with Progressive Solidification

Amiruddin[*], Shinji SASSA[**] and Hideo SEKIGUCHI

* Graduate School of Engineering, Kyoto University
** Port and Airport Research Institute, 3-1-1 Nagase, Yokosuka

Synopsis

The flow-out potential of a body of fluidized sediment following abrupt collapse is discussed through numerical and physical modelling. The emphasis of the analysis procedure is placed on considering the multi-phased nature of sediment gravity flows. Specifically, it combines Navier-Stokes/continuity equations for a liquefied soil domain with a consolidation equation for a solidifying soil domain. Evolutions of the flow and solidification surfaces are traced as part of solution by using a volume-of-fluid (VOF) technique. The physical modelling is concerned with two-dimensional flume tests, in which a column of fluidized sandy sediment was subjected to abrupt collapse and then allowed to flow out into ambient water. The observed and calculated results show that the sediment flow manifests itself as a decelerating gravity flow due to interactions between the flowing liquefied soil and the underlying soil with grain-supported framework being reestablished. Furthermore, a three-dimensional analysis is worked out for a class of levee breaching problems, with the aim of clarifying spread characteristics of flood water through the breached section.

Keywords: fluidization, progressive solidification, re-deposition, sediment gravity flow, three-dimensional analysis

1. Introduction

Sediment gravity flows under water have become an increasingly important subject for research in relation to geomorphodynamics of sediment routing systems that connect river basins, estuaries and coastal oceans. Also, submarine landslides and flow slides have received considerable practical attention in view of their destructive power and associated consequences in nearshore and offshore facilities (Hampton et al. 1993). Fluid-sediment interactions are a key process that features any of subaqueous sediment gravity flows. Thus integration of fluid-dynamics and soil-mechanics approaches will be indispensable in advancing the physics of subaqueous sediment gravity flows. It is of interest in this regard to note that the importance of pore water pressure in the dynamics of debris flows was pointed out by Iverson (1997).

This study aims at developing an analysis framework that facilitates a better understanding of complex fluid-sediment interactions which may occur in low-lying waterfront areas during extreme events. Breaching of a levee section at flood stage, for example, may bring about serious consequences in the immediately adjacent area and beyond, particularly when urbanization has already progressed to a significant extent. Serious erosion and sedimentation hazards may occur on sloping beaches due to severe storm waves,

notably in the form of large-scaled, rapid movement of particulate sediments across the shoreline.

With the above-mentioned in mind, this paper focuses the discussion on the dynamics of sediment-water mixtures that may result from failures of water-retaining soil structures or of nearshore granular slopes. More specifically, it investigates into the way in which a body of liquefied or fluidized sediment flows out, spreads and comes to re-deposition. This approach attempts to emphasize the multi-phased nature of sediment gravity flows and leads to expounding a computational code for liquefied sediment flows (LIQSEDFLOW). The computational code was initially developed for a two-dimensional analysis (Sassa et al., 2003) and has recently been extended for facilitating a three-dimensional analysis (Amiruddin et al., 2004).

In what follows, the theoretical background to the computational codes will first be outlined. A discussion will then be made of the performance of numerical and physical modelling of subaqueous sediment gravity flows following fluidization. A three-dimensional analysis will then be worked out, with the aim of shedding some light on the consequence of abrupt collapse of a levee section at flood stage.

2. Theory of subaqueous liquefied sediment flow with solidification

2.1 Problem definition

Consider a body of submerged granular soil that has just undergone liquefaction or fluidization under the action of storm waves, currents or excessive seepage forces. The liquefied sediment, with a mass density ρ_2, will start collapsing under gravity into an ambient fluid with a mass density ρ_1. The depth of the ambient fluid is assumed here to be constant in the course of flowage. A snapshot of the flowing entire system under consideration is schematically shown in Fig. 1. In the course of the liquefied sediment flow, the solidification should occur from the bottom of the liquefied soil layer and develop such that the solidification front, z_S, will progress upwards (Miyamoto et al., 2004a, b).

The pore fluid pressure p at a generic point in the sediment may be divided into two components. Namely,

$$p = p_e + p_s \qquad (1)$$

where p_s is the hydrostatic pressure which is expressed as $p_s = \rho_1 g(h-z)$, and p_e represents the excess

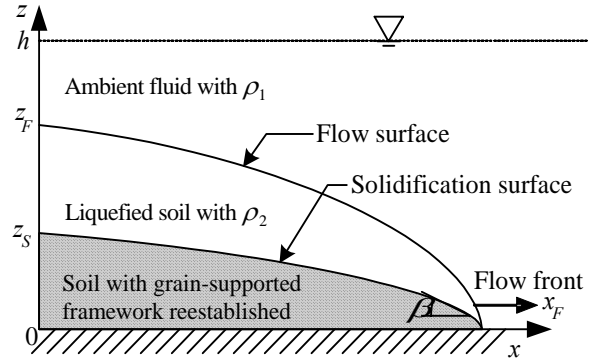pressure due to contractancy (i.e., tendency for volume reduction under shearing) of the sediment.

Fig. 1 Flow stratification with two moving interfaces

2.2 Formulation for the domain of liquefied flow

Consider a body of liquefied soil underwater. One of the simplest yet meaningful modelling for the liquefied soil is to regard it as a heavy, incompressible viscous fluid with a free surface. There follow

$$\frac{\partial u}{\partial x} + \frac{\partial v}{\partial y} + \frac{\partial w}{\partial z} = 0 \qquad (2)$$

$$\frac{\partial u}{\partial t} + u\frac{\partial u}{\partial x} + v\frac{\partial u}{\partial y} + w\frac{\partial u}{\partial z} =$$
$$-\frac{1}{\rho_2}\frac{\partial p_e}{\partial x} + \nu\left(\frac{\partial^2 u}{\partial x^2} + \frac{\partial^2 u}{\partial y^2} + \frac{\partial^2 u}{\partial z^2}\right) \qquad (3a)$$

$$\frac{\partial v}{\partial t} + u\frac{\partial v}{\partial x} + v\frac{\partial v}{\partial y} + w\frac{\partial v}{\partial z} =$$
$$-\frac{1}{\rho_2}\frac{\partial p_e}{\partial y} + \nu\left(\frac{\partial^2 v}{\partial x^2} + \frac{\partial^2 v}{\partial y^2} + \frac{\partial^2 v}{\partial z^2}\right) \qquad (3b)$$

$$\frac{\partial w}{\partial t} + u\frac{\partial w}{\partial x} + v\frac{\partial w}{\partial y} + w\frac{\partial w}{\partial z} =$$
$$-\frac{1}{\rho_2}\frac{\partial p_e}{\partial z} + \nu\left(\frac{\partial^2 w}{\partial x^2} + \frac{\partial^2 w}{\partial y^2} + \frac{\partial^2 w}{\partial z^2}\right) \qquad (3c)$$

where u, v and w are the velocities in x, y and z directions, g is the gravitational acceleration and ν is the kinematic viscosity.

2.3 Formulation for the domain undergoing solidification

The progress of solidification in the course of the liquefied flow may be effected by three-dimensional consolidation. There follow

$$\frac{\partial(\sigma_m - p_e)}{\partial t} = -\frac{kM}{\rho_1 g}\left(\frac{\partial^2 p_e}{\partial x^2}\right.$$
$$\left. + \frac{\partial^2 p_e}{\partial y^2} + \frac{\partial^2 p_e}{\partial z^2}\right) \qquad (4)$$

For the purpose of non-dimensional formulation, let

us introduce a reference length H and a reference velocity $U_r = \sqrt{gH}$. The non-dimensional time T may then be expressed as $U_r t/H$, and the non-dimensional excess pore pressure P_e may be expressed as $p_e/(\rho_2 - \rho_1)U_r^2$. Let K be the Darcy permeability coefficient, which is non-dimensionalized by dividing by U_r. Let M be the bulk modulus of the soil skeleton, which is non-dimensionalized by dividing by $(\rho_2 - \rho_1)U_r^2$. The consolidation equation then reads:

$$\frac{\partial^2 P_e}{\partial X^2} + \frac{\partial^2 P_e}{\partial Y^2} + \frac{\partial^2 P_e}{\partial Z^2} = -\frac{1}{\rho' MK}\frac{\partial(\sigma_m - P_e)}{\partial T} \qquad (5)$$

where $\rho' = (\rho_2 - \rho_1)/\rho_1$ and σ_m is the normalized mean total stress of the solidifying particulate sediment.

2.4 Numerical method

(1) Finite-difference approximations to storage equation

The solution procedure developed in this study is applicable not only to the prediction of progressive solidification, but also to the prediction of a precursory process of liquefaction. Since a solution procedure for liquefaction was described in detail by Amiruddin *et al.* (2004), we shall subsequently concentrate on the procedure for solving equation (5) for solidified soil.

For the purpose of solving equation (5) under moving boundary conditions, we adopted an implicit finite-difference scheme. A standard finite-difference approximation to equation (5) in MAC-type methods is expressed as

$$\begin{aligned}
&\left[\frac{1}{\Delta x_i}\left(\frac{P_{i+1,j,k}^{n+1} - P_{i,j,k}^{n+1}}{\Delta x_{i+1/2,j,k}} - \frac{P_{i,j,k}^{n+1} - P_{i-1,j,k}^{n+1}}{\Delta x_{i-1/2,j,k}}\right)\right.\\
&+ \frac{1}{\Delta y_j}\left(\frac{P_{i,j+1,k}^{n+1} - P_{i,j,k}^{n+1}}{\Delta y_{i,j+1/2,k}} - \frac{P_{i,j,k}^{n+1} - P_{i,j-1,k}^{n+1}}{\Delta y_{i,j-1/2,k}}\right)\\
&\left.+ \frac{1}{\Delta z_k}\left(\frac{P_{i,j,k+1}^{n+1} - P_{i,j,k}^{n+1}}{\Delta z_{i,j,k+1/2}} - \frac{P_{i,j,k}^{n+1} - P_{i,j,k-1}^{n+1}}{\Delta z_{i,j,k-1/2}}\right)\right] =\\
&-\frac{1}{\rho' MK}\left[\frac{\sigma_m^{n+1} - \sigma_m^n}{\Delta t} - \frac{P_{i,j,k}^{n+1} - P_{i,j,k}^n}{\Delta t}\right]
\end{aligned} \qquad (6)$$

In equation (6), we represent P_e by P. Equation (6) can be written as

$$\begin{aligned}
&A_1 P_{i+1,j,k}^{n+1} + A_2 P_{i-1,j,k}^{n+1} + A_3 P_{i,j+1,k}^{n+1}\\
&+ A_4 P_{i,j-1,k}^{n+1} + A_5 P_{i,j,k+1}^{n+1} + A_6 P_{i,j,k-1}^{n+1}\\
&- A_7 P_{i,j,k}^{n+1} = Q_{i,j,k}^n
\end{aligned} \qquad (7)$$

where

$$A_1 = 1/(\Delta x_i \Delta x_{i+1/2}); \qquad A_2 = 1/(\Delta x_i \Delta x_{i-1/2})$$
$$A_3 = 1/(\Delta y_j \Delta y_{j+1/2}); \qquad A_4 = 1/(\Delta y_j \Delta y_{j-1/2})$$
$$A_5 = 1/(\Delta z_k \Delta z_{k+1/2}); \qquad A_6 = 1/(\Delta z_k \Delta z_{k-1/2})$$
$$A_7 = A_1 + A_2 + A_3 + A_4 + A_5 + A_6 + A_{RHS}$$
$$A_{RHS} = 1/(\rho' MK\Delta t)$$
$$Q_{i,j,k}^n = -\left(\frac{\sigma_m^{n+1} - \sigma_m^n + P_{i,j,k}^n}{\rho' MK\Delta t}\right)$$

Here $\Delta x_{i+1/2} = (\Delta x_{i+1} + \Delta x_i)/2$, $\Delta y_{j+1/2} = (\Delta y_{j+1} + \Delta y_j)/2$ and $\Delta z_{k+1/2} = (\Delta z_{k+1} + \Delta z_k)/2$. The final matrix form to be solved with respect to equation (5) may be expressed as

$$AP = Q \qquad (8)$$

The simultaneous linear equations (8) were solved in this study using the Gauss-Jordan method.

(2) Computational procedure

The computational procedure for the entire system proceeds as follows (Fig. 2). The Navier-Stokes equations (3) for the liquefied soil in combination with continuity equation (2) may be solved using a finite difference method. Specifically, a simplified MAC method (Amsden and Harlow, 1970) in terms of staggered rectilinear grid was applied in this study. The associated Poisson equations regarding the excess pore pressures were solved using the Gauss-Jordan method. For tracking the flow surface a volume-of-fluid (VOF) technique (Hirt and Nichols, 1981) was applied, along with an efficient volume-advection scheme (Hamzah, 2001) so as to ensure the conservation of mass in the course of the liquefied flow. The evolution of the interface between the liquefied and solidifying soil domains was also traced using the VOF technique. More specifically, the soil undergoing solidification was treated as being an obstacle to the flowing liquefied soil, such that the velocities in the solidified soil become zero. This assumption is justifiable since the solidified zone should have a much higher stiffness and frictional resistance, compared with the liquefied soil.

Also, a transition layer of "structured liquefied soil" was introduced for dealing with the evolution of the solidification front (Miyamoto et al., 2004b). In essence, the transition layer occupies the lowermost part of the liquefied soil domain and immediately overlies the solidified soil domain. By doing so, one can realize the phase change that occurs in accordance with advancing

solidification front. Note that in a computational step, the solidification front may be judged to be an active one if the effective stress increment in the transition layer becomes positive. Then, the solidification front can move upwards by an amount equal to the prescribed thickness of the transition layer. Concurrently, the liquefied soil domain retreats by the same amount, and the transition layer assumes a new (higher) location. The slope of the solidification surface, β, may be modified, if necessary, so as not to exceed a critical angle β_{cr} in view of the frictional resistance of the soil.

Following a computational step, all variables are updated, the time and cycle counters are incremented and the computational cycle is restarted.

(3) Numerical stability

Numerical calculations often have computed quantities that develop large high-frequency oscillations in space and time. This behavior is usually referred to as numerical instability, especially if the physical problem has unstable solutions and if the calculated results exhibit significant variations over distances comparable to a cell width or over times comparable to the time increment. If this happens, the accuracy of the calculated results cannot be relied on. To prevent such numerical instability or inaccuracy, certain restrictions should be observed in defining the mesh increments, the time increment and the upstream differencing parameter α.

The mesh increments should be chosen small enough to resolve the expected spatial variations in all dependent variables. Once a mesh has been chosen, the choice of the time increment necessary for stability is governed by two restrictions. First, fluid must not flow across more than one computational cell in one time step because the finite difference equations assume fluxes only between adjacent cells. Thus, the time increment must satisfy the following inequality

$$\Delta t_{CFL} \langle \min\left\{\frac{C_r\Delta x}{|u|}, \frac{C_r\Delta y}{|v|}, \frac{C_r\Delta z}{|w|}\right\} \quad (9)$$

where the minimum is evaluated with respect to every cell in the mesh and C_r is a Courant number (Hirt and Nichols, 1981). Second, when a nonzero value of kinematic viscosity is used, the momentum must not diffuse more than approximately one cell in one time step. A linear stability analysis shows that this limitation implies

$$\nu\Delta t_{VIS} \langle \frac{1}{2}\frac{\Delta x^2\Delta y^2\Delta z^2}{\left(\Delta x^2 + \Delta y^2 + \Delta z^2\right)} \quad (10)$$

With Δt chosen to satisfy the above two inequalities, the last parameter needed to ensure numerical stability is α. The proper choice for α is

$$1 \geq \alpha \rangle \max\left\{\left|\frac{u\Delta t}{\Delta x}\right|, \left|\frac{v\Delta t}{\Delta y}\right|, \left|\frac{w\Delta t}{\Delta z}\right|\right\} \quad (11)$$

In the present computation code, the value of α is automatically adjusted to be:

$$\alpha = \min\left(1.2\max\left\{\left|\frac{u\Delta t}{\Delta x}\right|, \left|\frac{v\Delta t}{\Delta y}\right|, \left|\frac{w\Delta t}{\Delta z}\right|\right\}, 1\right) \quad (12)$$
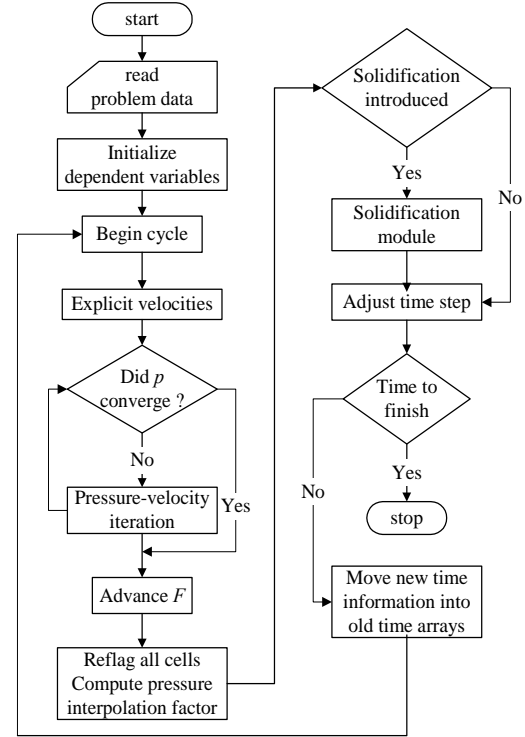

Fig. 2 Flowchart of the computer program

3. Modelling of two-dimensional subaqueous sediment gravity flows following fluidization

3.1 Experimental program

We performed a range of two-dimensional flume tests for looking at flow-out characteristics of particulate sediments following fluidization.

The flume used is 1.5 m long, 1.25 m deep and 0.05 m thick (Fig. 3a). The sand used is silica No. 6, which has the average grain size of 0.32 mm and the void ratio at loosest packing of 1.17. Three series of experiments were performed with relatively high concentrations, c, as listed in Tables 1 and 2. The first series put emphasis on looking at progressive solidification in fluidized sediment gravity flow. In this series, the value of the initial thickness of the sediment H_0 was varied such that the height of fluidized sand, H, became equal to 200mm.

The second series of experiments put emphasis on capturing deformed configurations of fluidized sediment. In this series, the initial height of sand deposit, H_0 was set equal to 150mm. The height of fluidized sand, H, was varied to give different concentrations, c. The third series of experiments were designed for capturing flowage of the fluidized sediment. In this series, the flowage conditions were kept essentially the same while the position of the CCD camera was varied as listed in the table.

The ambient water depth in each test was kept at 1.1m. A sand layer 5mm thick was placed on the floor of the channel in order to achieve realistic boundary conditions for the sediment gravity flow. The sediment was then subjected to upward seepage flow under a given discharge velocity, yielding a liquefied or fluidized state of sediment (refer to Fig. 4). Then, the release gate was swiftly opened, allowing the sediment to flow out over a horizontal floor in the channel.

The movement of the flow surface was observed using a digital video camera. The movement of the sediment was captured using a high-speed CCD camera (recording rate: 125 frames/s; shutter speed: 1/1000 s and resolution: 640×240 pixels). The use of particle image velocimetry (PIV) technique (Kimura et al., 2001) provided a useful dataset regarding the evolution of the velocity field in the sediment gravity flow underwater.

The changes in water pressure were measured with four pore-pressure transducers (PPTs). The PPTs were fixed in space using attachments that were connected to the wall of the flume (Fig. 3b).
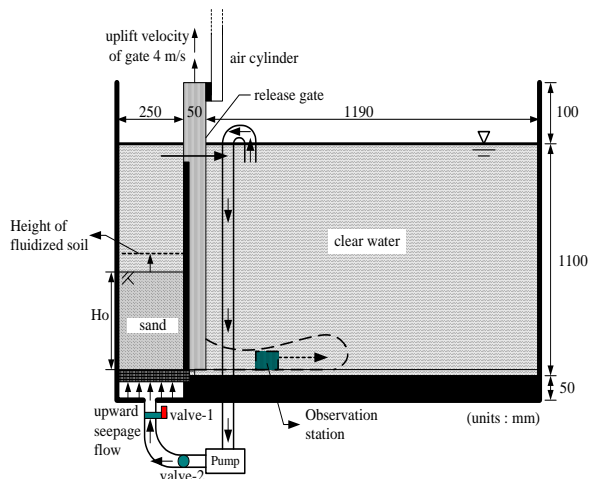
Fig. 3 Setup for experiment on sediment gravity flow following fluidization

3.2 Characteristics of sediment gravity flow

Snapshots of sediment gravity flows at four stages are shown in Fig. 5 in four tests of the second series of experiments. For purposes of comparisons, a column of water in air was allowed to collapse under its own weight. The flowage pattern is illustrated in Fig. 6. These pictures were taken using the digital video camera with the frame rate equal to 1/30 seconds.

The measured time histories of locations of the head of sediment gravity flows are shown in Fig. 7 for the four different volumetric concentrations c indicated. In this figure, the measured performance of the gravity flow of water is also plotted. It is seen that the gravity flow of water exhibited nearly constant rate of flow until the flow head hit the downstream end of the channel. By contrast, the sediment gravity flows underwent decelerating flowage, except for the early stage of flow initiation.

The measured time histories of water pressure changes in the first series of experiments are shown in Appendix of this paper.
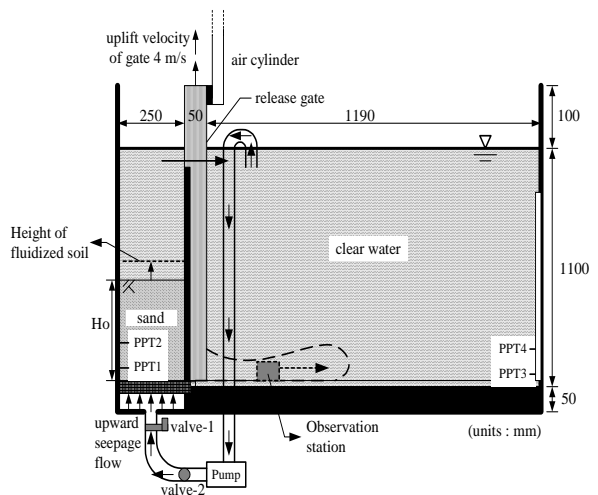

Fig. 3b Setup for experiment on sediment gravity flow following fluidization, with four PPTs installed
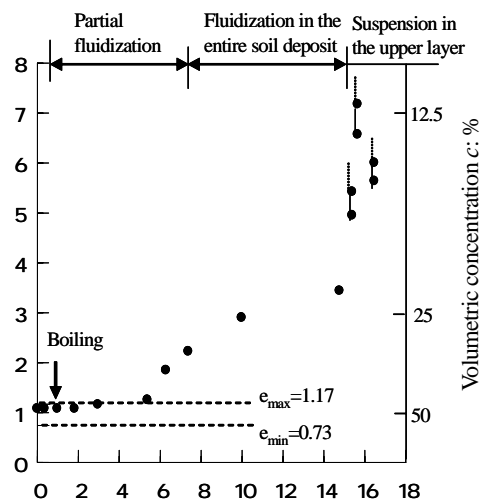

Fig. 4 Void ratios of sediment plotted against imposed vertical seepage velocities, showing transformation of the state of sediment

Table 1 Test conditions for experiments on sediment gravity flow.

Test number	Concentration c (%)	Mass of dry sand M_s (gr)	Height (mm)		Void ratio		Density ρ (kg/m^3)	Position of PPTs from the gate (mm)	Position of CCD from the gate (mm)
			H_0	H	e_0	e			
First Series									
PPTFLOW-1	42	3030	182	200	1.14	1.35	1702	600	100
PPTFLOW-2A	38	2700	164	200	1.15	1.61	1632	1150	100
PPTFLOW-2B	38	2700	164	200	1.15	1.61	1632	600	150
PPTFLOW-3A	34	2420	147	200	1.15	1.88	1573	1150	100
PPTFLOW-3B	34	2420	147	200	1.15	1.88	1573	600	150
PPTFLOW-4A	30	2130	129	200	1.15	2.25	1508	1150	100
PPTFLOW-4B	30	2420	129	200	1.15	2.25	1508	600	150
Second Series									
DVFLOW-1	42	2500	150	163	1.13	1.34	1704		
DVFLOW-2	38	2500	150	183	1.14	1.61	1632		
DVFLOW-3	34	2500	150	202.3	1.15	1.91	1566		
DVFLOW-4	30	2500	150	202.5	1.15	2.33	1495		

Table 2 Test conditions for experiments on sediment gravity flow for differing stations with the single CCD-camera

| Test number	Concentration c (%)	Mass of dry sand M_s (gr)	Height (mm)		Void ratio		Position of CCD from the gate (mm)
			H_0	H	e_0	e	
Third Series							
PPTCCD-1	38	2700	163	200	1.13	1.61	0
PPTCCD-2	38	2700	164	200	1.14	1.61	50
PPTCCD-3	38	2700	165	200	1.15	1.61	200
PPTCCD-4	38	2700	164	200	1.14	1.61	250
PPTCCD-5	38	2700	164	200	1.14	1.61	300
PPTCCD-6	38	2700	165	200	1.15	1.61	350
PPTCCD-7	38	2700	165	200	1.15	1.61	400
PPTCCD-8	38	2700	166	200	1.16	1.60	450
PPTCCD-9	38	2700	165	200	1.15	1.61	500
PPTCCD-10	38	2700	165	200	1.15	1.61	550
PPTCCD-11	38	2700	164	200	1.14	1.61	600
PPTCCD-12	38	2700	164	200	1.14	1.61	650
PPTCCD-13	38	2700	165	200	1.15	1.61	700
PPTCCD-14	38	2700	165	200	1.15	1.61	750
PPTCCD-15	38	2700	166	200	1.16	1.60	800
PPTCCD-16	38	2700	163	200	1.13	1.61	850
PPTCCD-17	38	2700	165	200	1.15	1.61	900
PPTCCD-18	38	2700	164	200	1.14	1.61	950
PPTCCD-19	38	2700	164	200	1.14	1.61	1000
PPTCCD-20	38	2700	164	200	1.14	1.61	1050
PPTCCD-21	38	2700	165	200	1.15	1.61	1100
PPTCCD-22	38	2700	166	200	1.16	1.60	1150
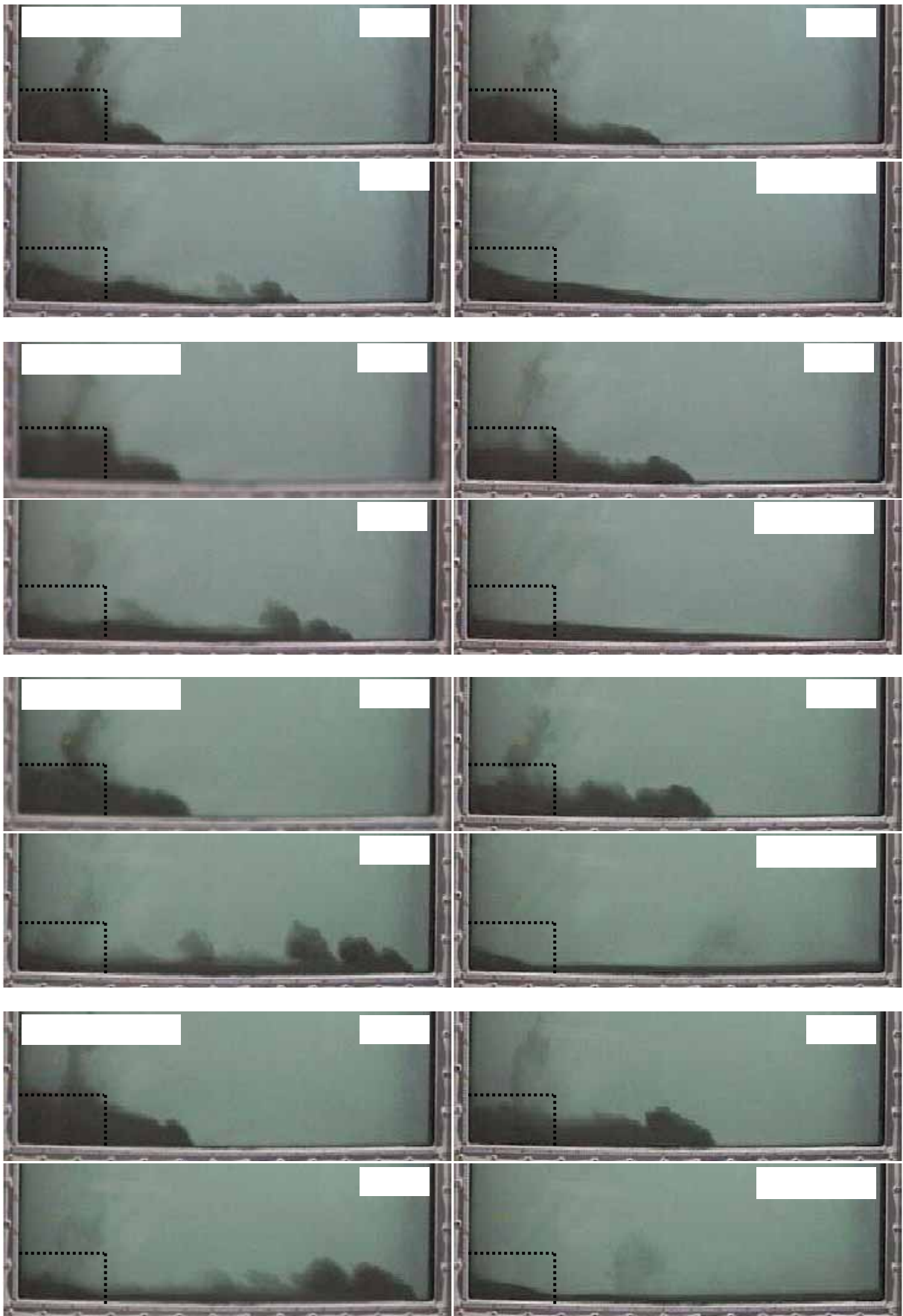
Fig. 5 Photographs of sediment gravity flows at four stages in four tests of the second series of experiments (····· represent initial configuration)
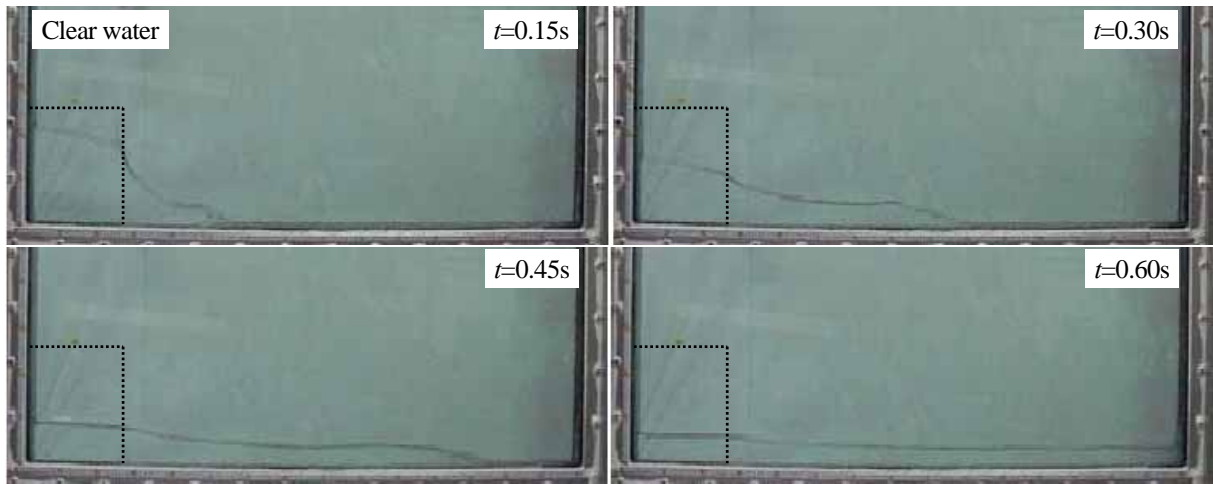
Fig. 6 Photographs showing collapse a column of water in air due to abrupt release of the gate
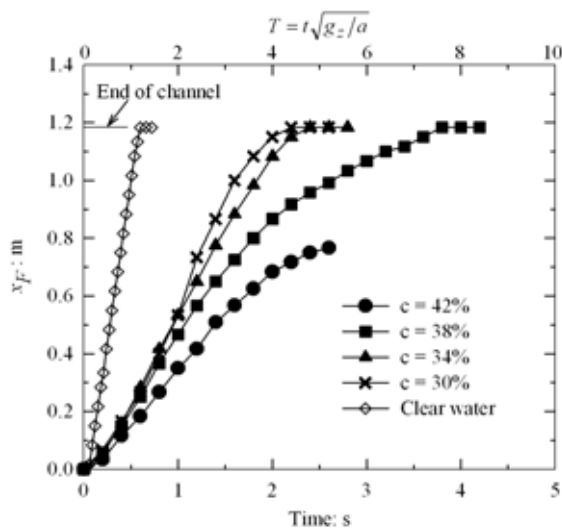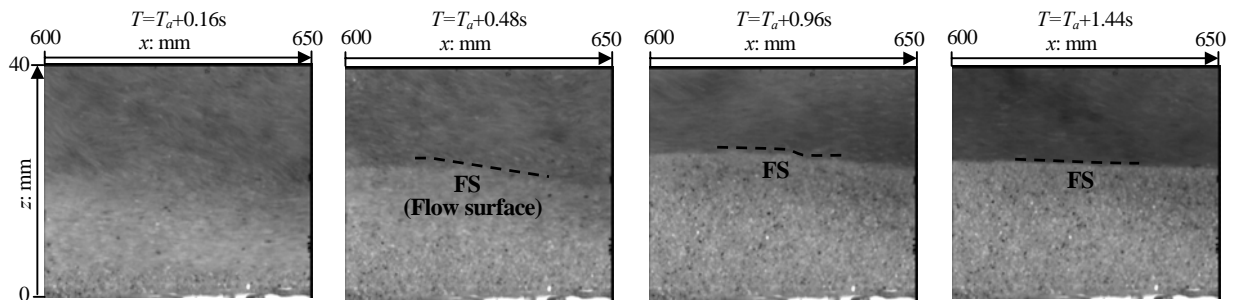

Fig. 7 Measured time histories of location of gravity flow head in second series of experiment

3.3 Progressive solidification in fluidized sediment gravity flow

Snapshots of sediment gravity flow in test PPTCCD-11 are shown in Fig. 8(a) for four different times indicated. Here, T_a represents the instant of time when the flow head just arrived at the station of

observation (x=650mm). The flow surface (FS) became apparent 0.48 seconds after the gravity flow head passed the observation station, and thereafter the flow surface became clearer. However, those raw images alone were insufficient to provide information regarding the evolution of solidification that occurred during flowage.

In fact, we found it practical to process those images in terms of the PIV technique. Use was made of the cross-correlation pattern matching technique which involved two consecutive images with a time spacing of $N\Delta t$. Here, Δt related to the frame rate of the high-speed CCD camera and was equal to 1/125 seconds. The value of N was chosen at 1. The velocity fields thus obtained are typified in Fig. 8(b), revealing the development of solidification zones during flowage. Note that the region with zero velocities spreads upwards as time elapses, indicating the occurrence of progressive solidification during flowage. The upper boundary of the solidification zone is called the solidification front (SF). The solidification front actually is a moving interface between the zone of completely fluidized sediment and the zone with a grain-supported framework being reestablished.

T_a: Instant of time when the flow head arrived at the station of observation (x=650mm)

Fig. 8 (a) Snapshots of fluidized sediment gravity flow (test PPTCCD-11) from a fixed station using the high-speed CCD camera
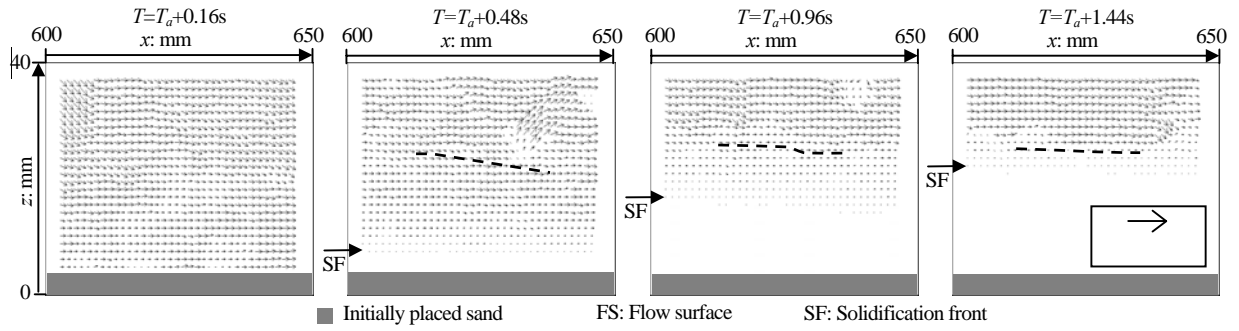
Fig. 8 (b) Velocity fields of sediment gravity flow in test PPTCCD-11 obtained through PIV technique, showing upward advance of solidification front

Table 3 Principal parameters in analyses for sediment gravity flow.

Simulation number	Concentration c (%)	b/a	Re	K	M	$\tan \beta_{cr}$	$(\rho_2 - \rho_1)/\rho_1$
Simulation-I							
Run-I-1	42	0.66	3.8×10^5	0.001	400	0.2	0.702
Run-I-2	42	0.66	3.8×10^5	0.001	400	0.3	0.702
Run-I-3	42	0.66	3.8×10^5	0.001	400	0.4	0.702
Run-I-4	42	0.66	3.8×10^5	0.001	400	0.5	0.702
Run-I-5	42	0.66	3.8×10^5	0.001	400	0.6	0.702
Simulation-II							
Run II-1	42	0.66	3.8×10^5	0.001	400	0.3	0.704
Run II-2	38	0.73	3.8×10^5	0.001	400	0.3	0.632
Run II-3	34	0.81	3.8×10^5	0.001	400	0.3	0.566
Run II-4	30	0.93	3.8×10^5	0.001	400	0.3	0.495

Let us now look at flow configurations of initially fluidized sediment with c=38% at the four elapsed times indicated (Fig. 9). This representation was made possible by performing a total of twenty-four identical flume tests and by assembling pictures taken from the twenty-four differing stations with the single CCD-camera. A close look at Fig. 9 permits one to grasp the movement of the head of the gravity flow. Also, it facilitates the application of the PIV technique for differing stations that correspond to differing travel distances.

Results of such image processing are typified in Fig. 10. It may readily be seen that as soon as the head of the gravity flow went past a given station, solidification started developing at that station from the base up, eventually reaching the flow surface. It is interesting to note that at the three stations under discussion, the solidification front reached the flow surface essentially the same instant of time. This suggests the occurrence of "freezing" of the main body of the sediment gravity flow.

3.4 Comparison between predicted and measured performances

A series of analyses were performed using LIQSEDFLOW in light of the experimental program described above. Two series of simulations were carried out as listed in Table 3. Simulations-I put emphasis on looking at the effect of varying $\tan \beta_{cr}$ upon flowage of sediment gravity flow. In this series of simulations, a relative column height $b/a = 0.66$ was used along with c=42%. Here a and b respectively denote the column width and height. Simulations-II were designed for comparing predicted and measured speeds of gravity flow head. A computational domain, 10 units horizontal by 2.5 units vertical, was discretized into a total of 100 by 25 grids. A regular interval $\Delta X = 0.1$ was applied in X-direction, and a variable grid was used in Z-direction with a minimum grid $\Delta Z = 0.01$ near the bottom of the computational domain. The variables used in the computations were all non-dimensional variables by choosing a as a reference length and $\sqrt{g_z a}$ as a reference velocity. The non-dimensional kinematic viscosity $v/a\sqrt{g_z a}$ was equal to 2.6×10^{-6}, giving rise to $Re = 3.8 \times 10^5$. The non-dimensional time increment $\Delta T = \Delta t \sqrt{g_z a}$ was taken as 0.001. Here g_z is gravitational acceleration. In the problem under discussion a rectangular column of heavy fluid (liquefied soil) was initially confined between a vertical wall and a gate, and was kept in hydrostatic equilibrium. Gravity
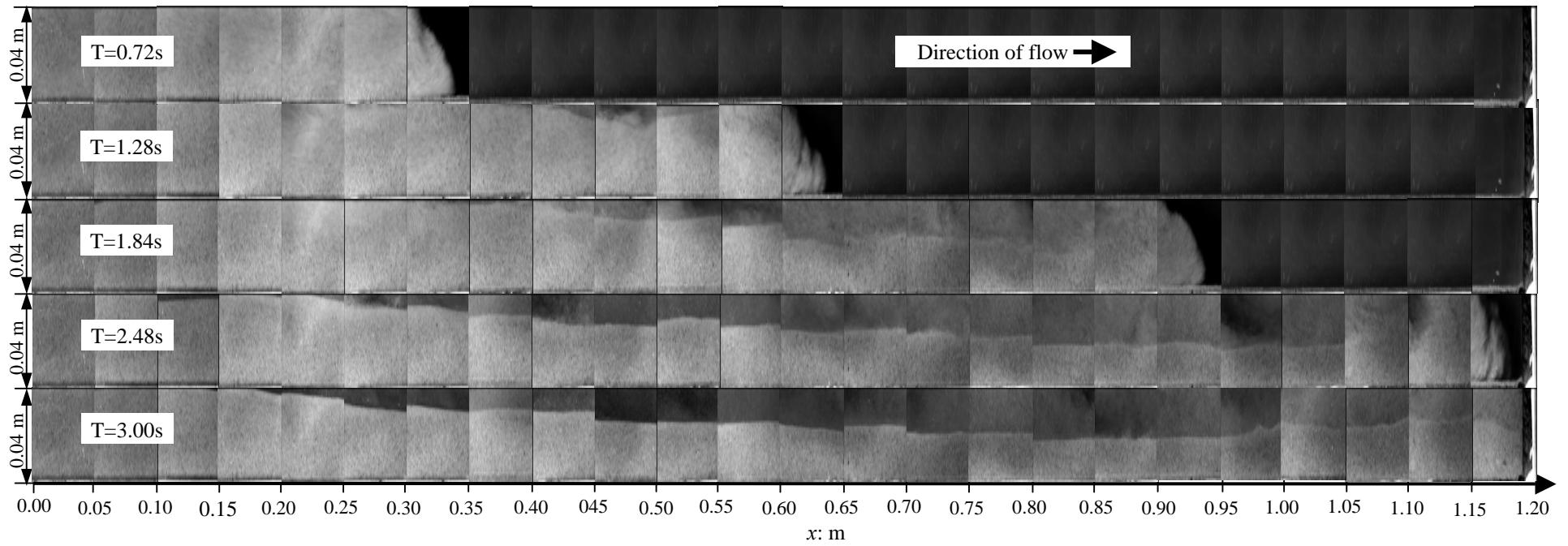
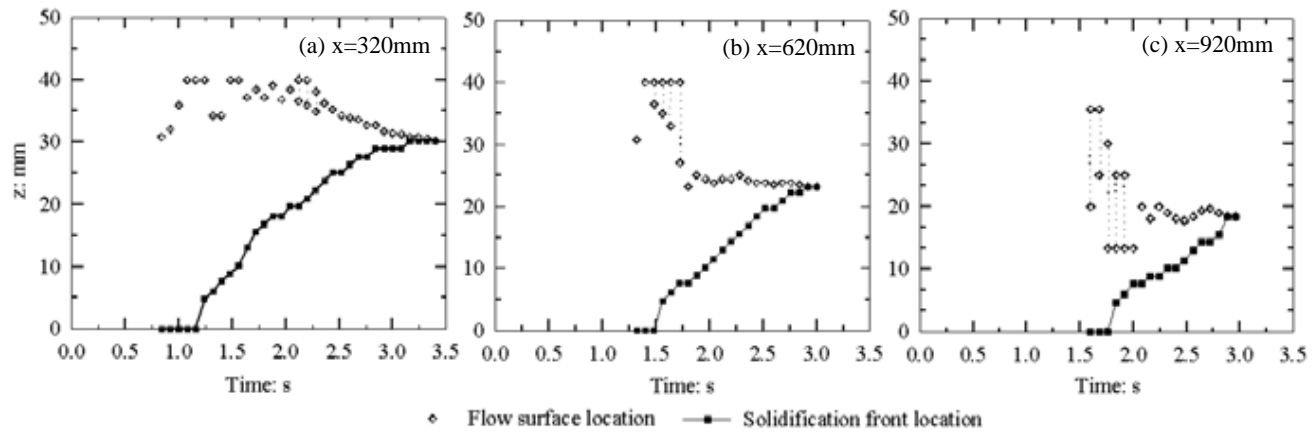Fig. 9 Flow configurations of initially fluidized sediment with c=38% at four elapsed times indicated

Fig. 10 Evolutions of flow surface and solidification front at three different stations in sediment gravity flow (c=38%)

with a unit magnitude was applied downwards. At the beginning of the calculation, the release gate was instantaneously removed and the dense fluid (liquefied soil) in the reservoir was allowed to flow out onto a horizontal floor.

The time histories of the location of gravity flow head of water (a=0.25m, b=0.25m) are shown in Fig. 11. It is seen that the predicted performance compares favourably with the observed flow behaviour until the time reached 0.5s or so. In Fig. 11 the experimental results of Martin and Moyce (1952) with a=0.06m, b=0.06m are also plotted, with the performance predicted by the present numerical scheme.
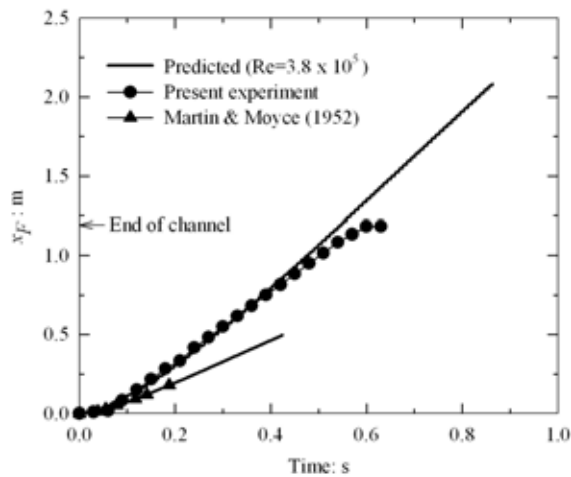
Fig. 11 Measured and predicted time histories of location of gravity flow head for clear water
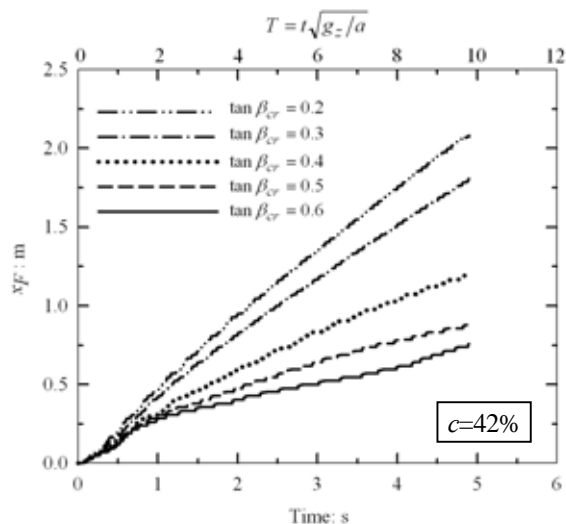
Fig. 12 Predicted time histories of location of gravity flow head for five different values of tan β_{cr}

The principal results from simulations-I are presented in Fig. 12. It is seen that flow potential of subaqueous sediment gravity flows decreases markedly with the increases in tan β_{cr}

The predicted changes in flow configuration of the

liquefied sediment with c=42% at a dimensionless time T=9.5 are shown in Fig. 13 for the five different values of tan β_{cr} indicated.
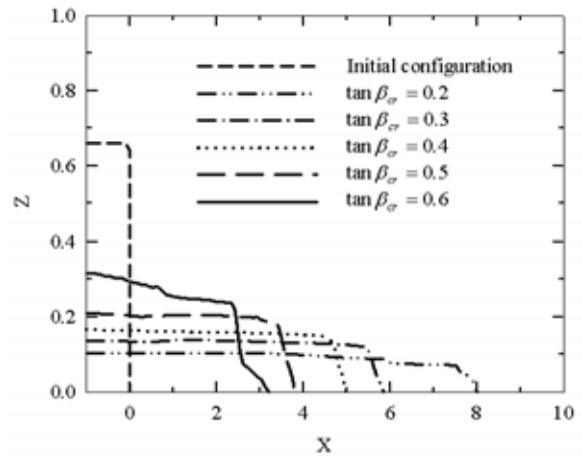
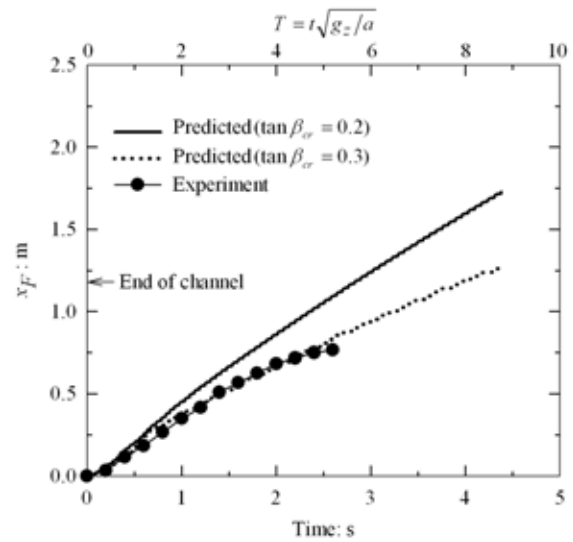Fig. 13 Predicted configurations of liquefied soil for c=42% at a dimensionless time T=9.5
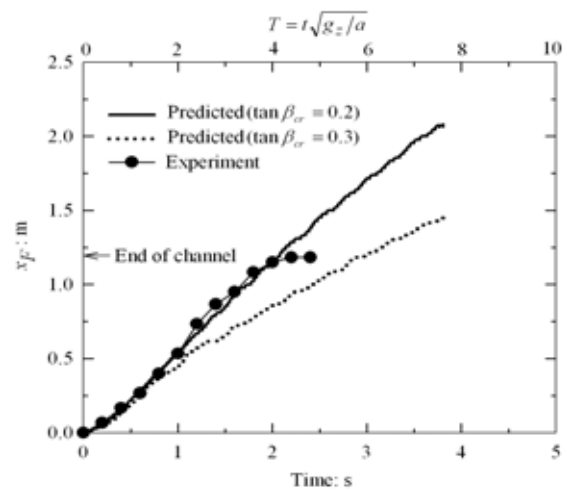
Fig. 14 (a) Predicted and measured time histories of location of gravity flow head for c= 30%
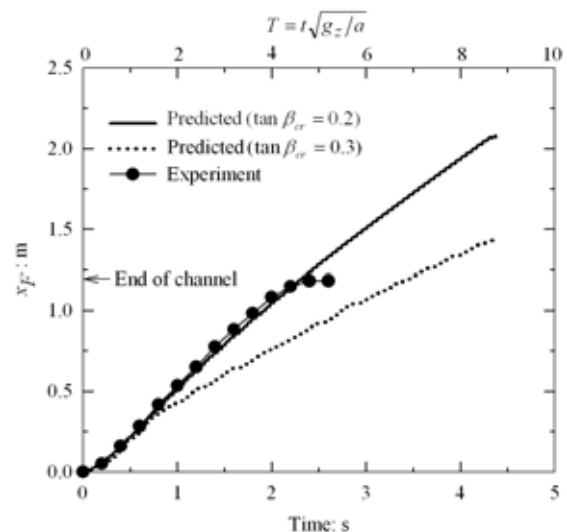
Fig. 14 (b) Predicted and measured time histories of location of gravity flow head for c= 34%
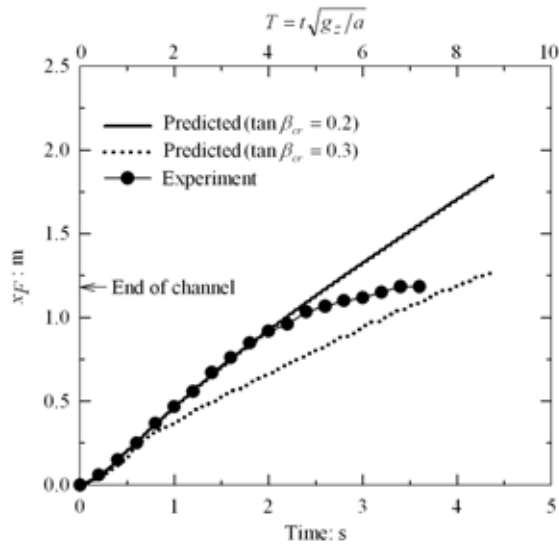
Fig. 14 (c) Predicted and measured time histories of location of gravity flow head for $c= 38\%$

The calculated time histories of the location of the gravity flow head for four different concentrations are shown in Figs. 14(a)-(d), together with the corresponding experimental results. It is seen that the predicted performance with $\tan\beta = 0.2$ compares favourably with the observed flow behaviour, for the cases with $c=30\%$, 34% and 38% in the early and intermediate stages of flowage. The observed performance for $c=42\%$ in Fig. 14(d) is of particular interest, because the flowage came to a complete stop. The predicted performance

with $\tan\beta = 0.3$ almost reproduced the flow pattern, but it could not reproduce the abrupt cessation of the flowage that was one of the most important aspect of the observed flow behaviour.

The predicted changes in the configuration of the liquefied sediment are illustrated in Fig. 15. Note that the sediment gravity flow underwent gradual solidification from the base up, thereby speeding down at a moderate rate in this particular calculation.

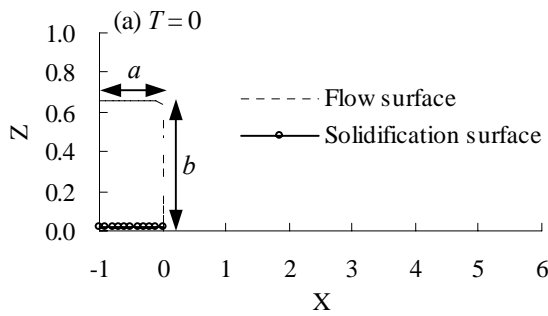Fig. 14 (d) Predicted and measured time histories of location of gravity flow head for $c= 42\%$
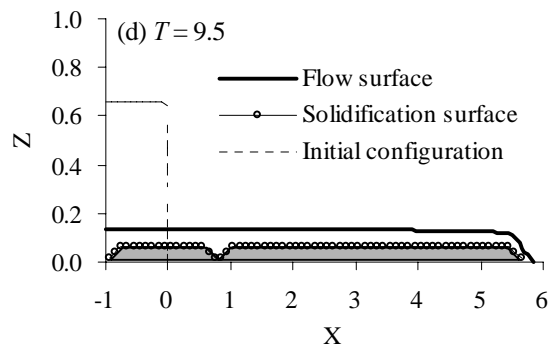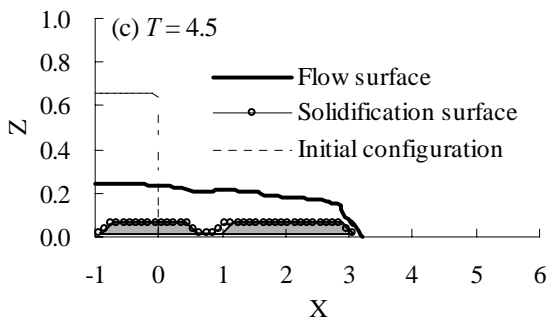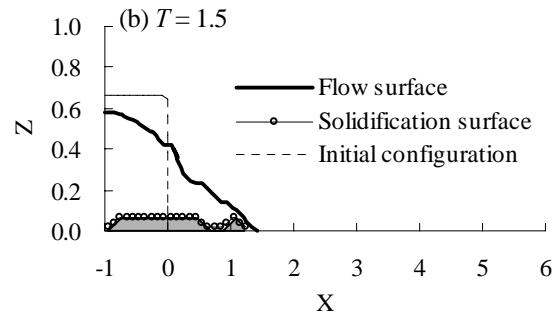
Fig. 15 Predicted flow configurations of liquefied soil with $c=42\%$ ($\tan\beta_{cr} = 0.3$) : (a) initial configuration (b) configuration at $T = 1.5$; (c) configuration at $T = 4.5$ and (d) configuration at $T = 9.5$

4. Analysis of three-dimensional levee breaching problem

This section discusses a class of levee breaching problems in terms of the three-dimensional version of LIQSEDFLOW. The definition of the problem taken up here is illustrated in Fig. 16. It is assumed that a 50-m wide section of a river levee undergoes abrupt collapse at flood stage, and the flood water thereafter starts flowing out toward the adjacent level ground. In order to keep the problem tractable, we neglect in the present analysis the incoming and outgoing flood flows in the river channel. No solidification during flowage is considered for simplicity.

A rectangular computational domain of 300m x 250m x 5.2m is subdivided into a non-uniform mesh that consists of 152 grids in the x-direction, 127 grids in the y-direction and 8 grids in the z-direction. A sort of gate 50 m wide, 2 m thick and 5.2 m high is provisioned in the computational domain so as to represent the breached section of a levee. The flood water is initially confined in the reservoir (enclosed river channel) and is thus stationary, as indicated in Fig. 16. The calculation starts upon abrupt removal of the gate and traces how the flood water flows out and spreads over the rigid, smooth, impermeable ground. The vertical profiles of the flowing water in the centerline at two representative times are depicted in Fig. 17. The deformed configuration of the free surface at $t = 50$s is illustrated in Fig. 18a, in terms of contours of equal elevations. An idea about the destructive power of rapidly flowing-out water may be obtainable by a close look at the velocity field such as demonstrated in Fig. 18b.
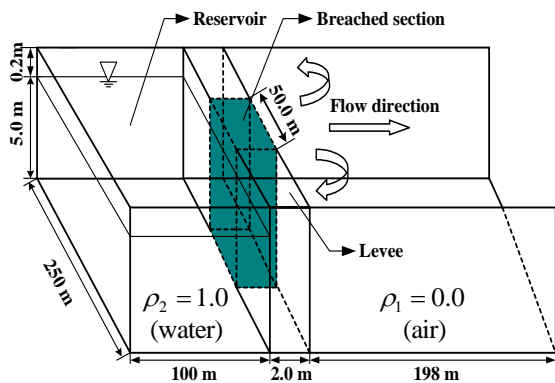

Fig. 16 Definition sketch for three-dimensional levee breaching problem

It is a subject for future study to relate the initial size and collapse rate of the breached section to the resulting velocity field of resulting gravity flow that spreads out in the flood plain. It is also of importance to look at the way in which overflows erode the outer portion of a levee section, allowing abrupt collapse of the levee section.
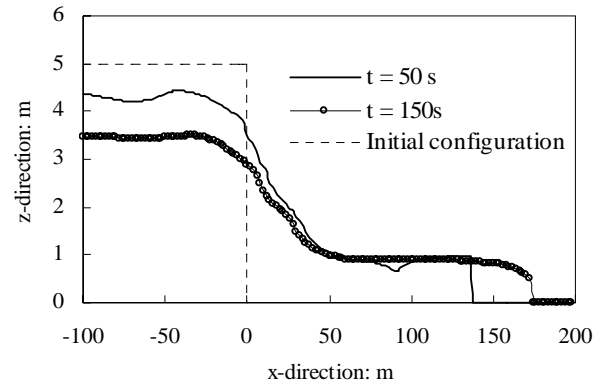

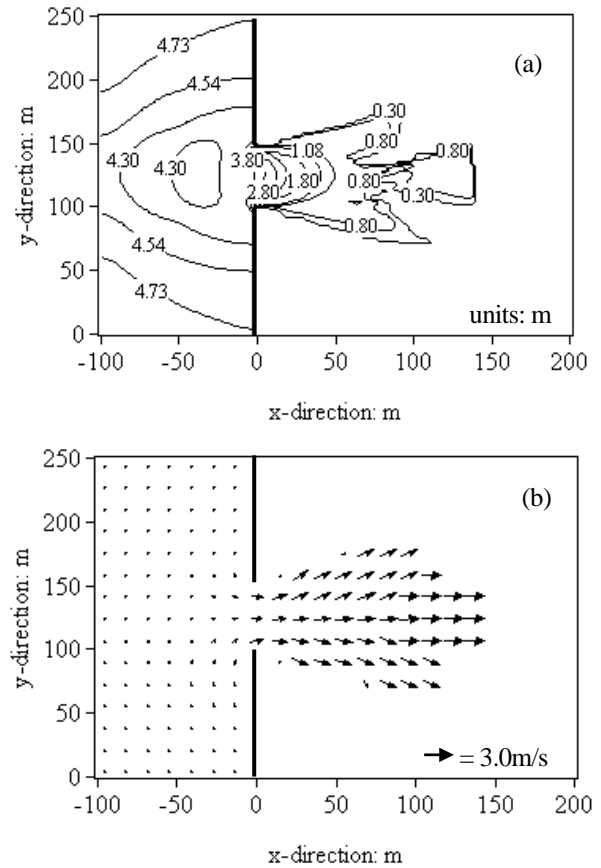Fig. 17 Predicted flow configurations

Fig. 18 Predicted flow-out pattern at t=50s: (a) contours of equal elevations in free surface; and (b) distributions of velocity vectors on a horizontal plane, $z = 1.0$m.

5. Conclusions

The flow-out potential of fluidized sediments as well as of flood water has been discussed in terms of the numerical and physical modelling. The principal conclusions derived are as follows:

1. The results from the two-dimensional flume tests show that subaqueous sediment gravity flows underwent marked decelerating regime, compared with the gravity flow of clear water. This aspect is reproduced fairly well by the present computational model.

2. The sediment gravity flow with c=42% was observed to speed down markedly in the later stage of flowage and it came to a stop, exhibiting what is called "freezing". This aspect may require more development in numerical modelling, such that full progress of solidification may be effected during flowage.

3. A three-dimensional levee breaching problem with flood stage is worked out, inspiring further advanced analysis and related field investigations.

References

Amiruddin, Sassa, S. and Sekiguchi, H., (2004). Analysis of three-dimensional sediment gravity flows, Annuals, DPRI, Kyoto University, No. 47 B, pp. 617-633.

Amsden, A.A. and Harlow, F.H., (1970). A simplified MAC technique for incompressible fluid flow calculations, J. Comput. Phys., 6: pp. 322-325.

Hampton, M. A., Lemke, R. W. and Coulter, H. W. 1993: Submarine landslides that had a significant impact on man and his activities; Seward and Valdez, Alaska. In: Submarine Landslides: Selected Studies in the U.S. Exclusive Economic Zone, 123-134.

Hamzah, M.A., (2001). Numerical simulations of tsunami pressure acting upon coastal barriers on wet and dry lands, Dr. Eng. Thesis, Kyoto University.

Hirt, C. W. and Nichols, B. D., (1981). Volume of fluid (VOF) method for the dynamics of free boundaries, J. Comput. Phys., 39: pp. 201-225.

Iverson, R. H. 1997. The physics of debris flows, Review of Geophysics, 35, No. 3, 245-296.

Kimura, I., Uemura, T. and Okuno, T., (2001). Visualization Techniques, Kindai-kagaku-sha publishing (in Japanese).

Martin, J. C. and Moyce. W.J. (1952): An experimental study of the collapse of liquid columns on a rigid horizontal plane, Phil. Trans. Roy. Soc. London A, Vol. 244, pp.312-324.

Miyamoto, J., Sassa, S., Tokuyama, R. and Sekiguchi, H. (2004a). Observations of the dynamics of subaqueous sediment gravity flows with progressive solidification, Annual Journal of Coastal Engineering, JSCE, Vol. 51 (1), pp. 401-405 (in Japanese).

Miyamoto, J., Sassa, S. and Sekiguchi, H. (2004b). Progressive solidification of a liquefied sand layer during continued wave loading, Geotechnique, Vol. 54 No. 10, pp. 617-629.

Sassa, S., Miyamoto, J. and Sekiguchi, H. (2003). The dynamics of liquefied sediment flow undergoing progressive solidification. In: Submarine Mass Movements and Their Consequences (eds. J. Locat and J. Mienart), Kluwer Academic Publishers, pp. 95-102.

Appendix

The measured time histories of water pressures in four tests of the first series of experiments are shown in Figs. A-1 through A-4. Enlarged views of water pressure changes after the release of the gate are shown in Fig. A-5 through A-8.
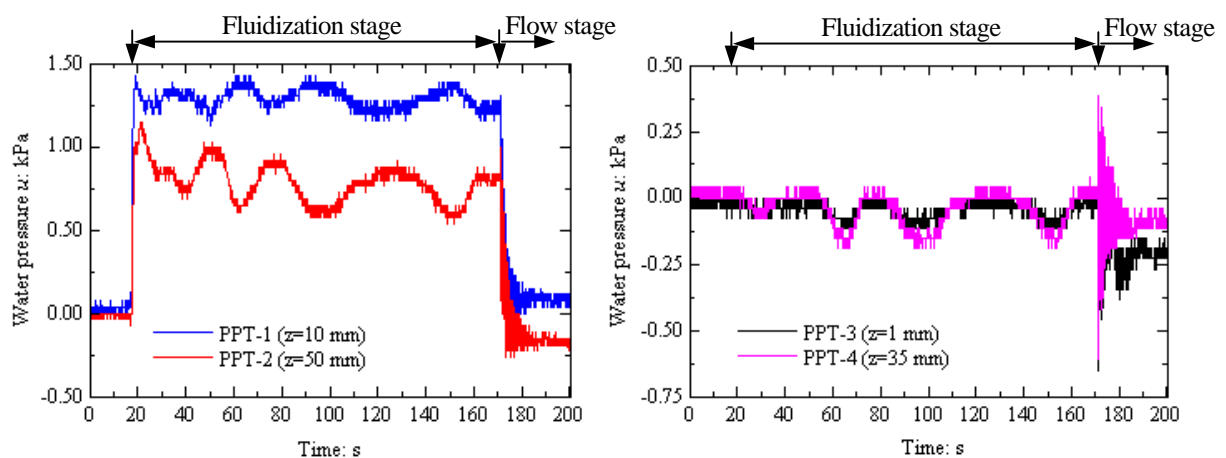

Fig. A-1 Measured time histories of water pressures in sediment gravity flow experiment (PPTFLOW-1)
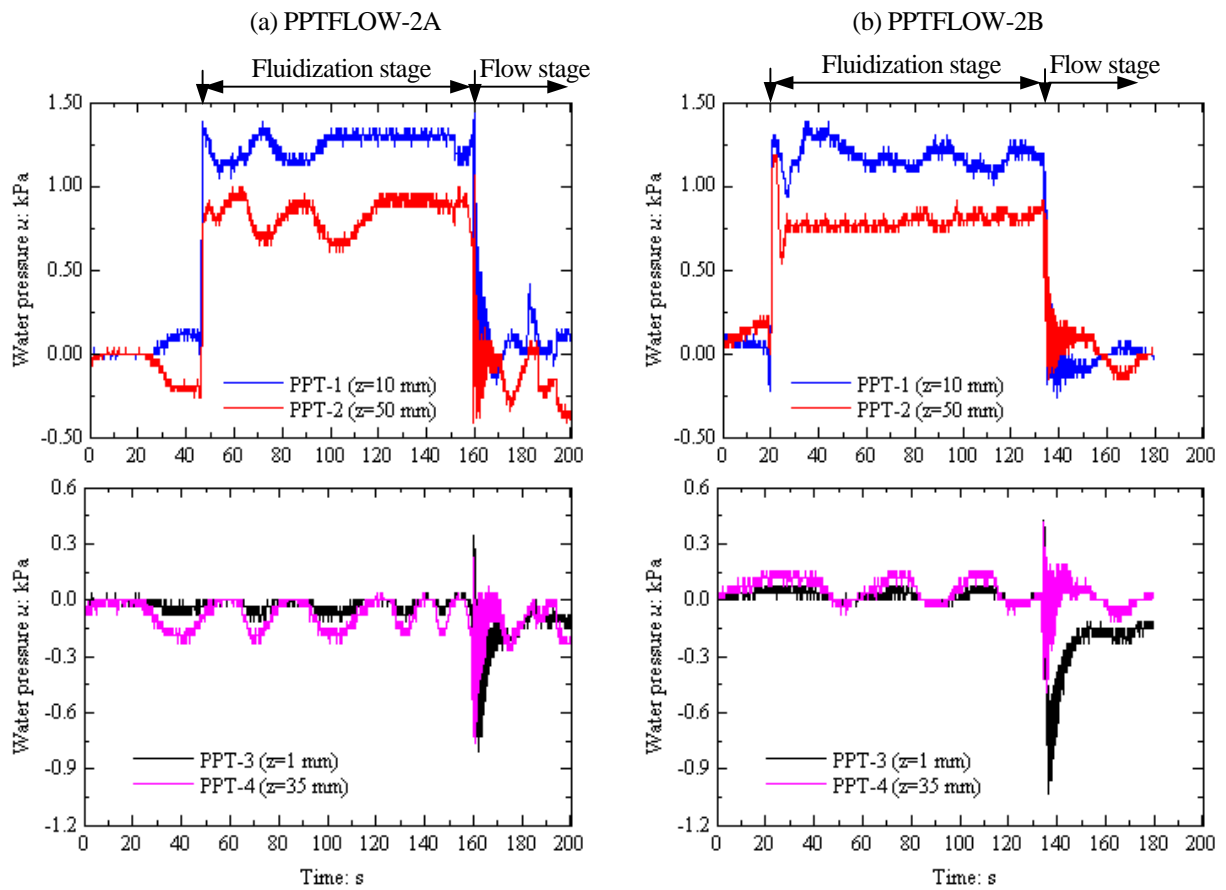
(a) PPTFLOW-2A

(b) PPTFLOW-2B

Fig. A-2 Measured time histories of water pressures in sediment gravity flow experiment (PPTFLOW-2)

(a) PPTFLOW-3A

(b) PPTFLOW-3B

Fig. A-3 Measured time histories of water pressures in sediment gravity flow experiment (PPTFLOW-3)
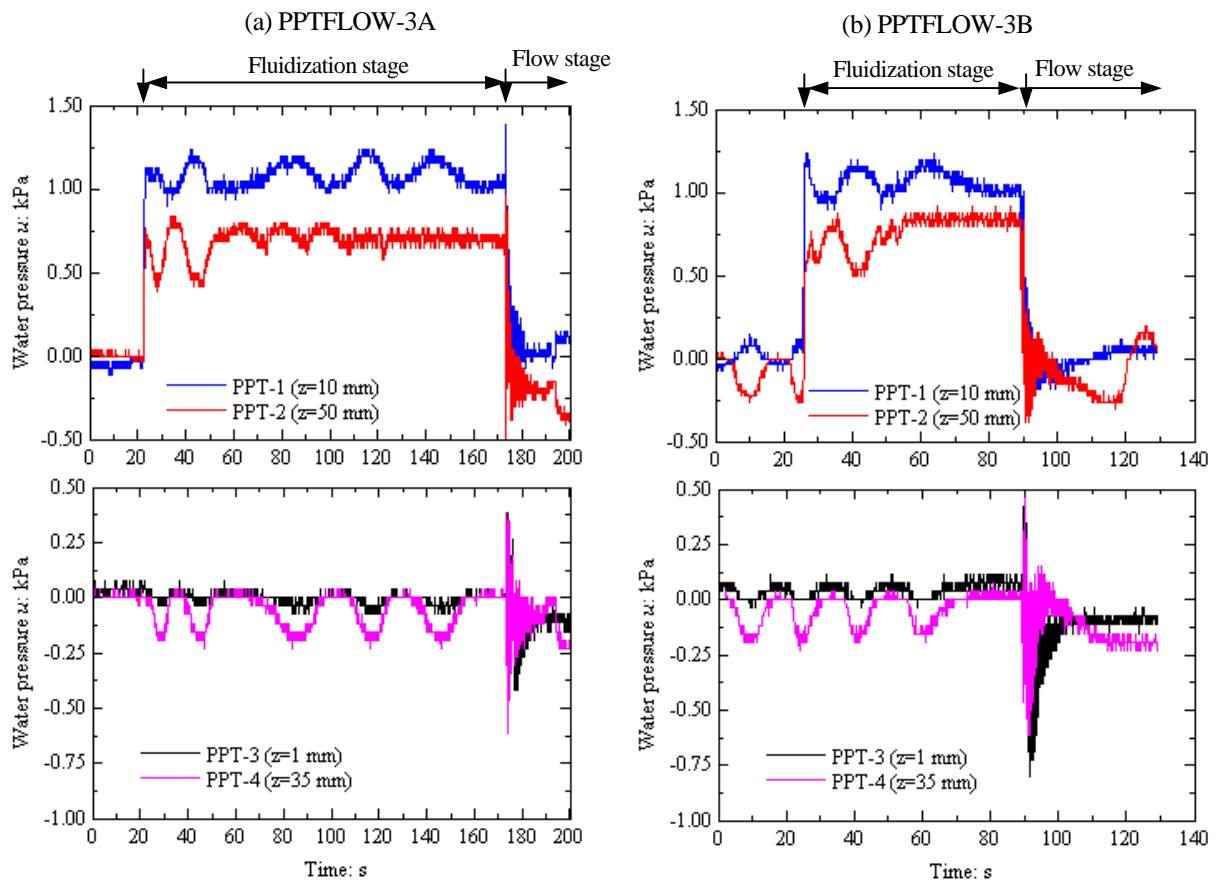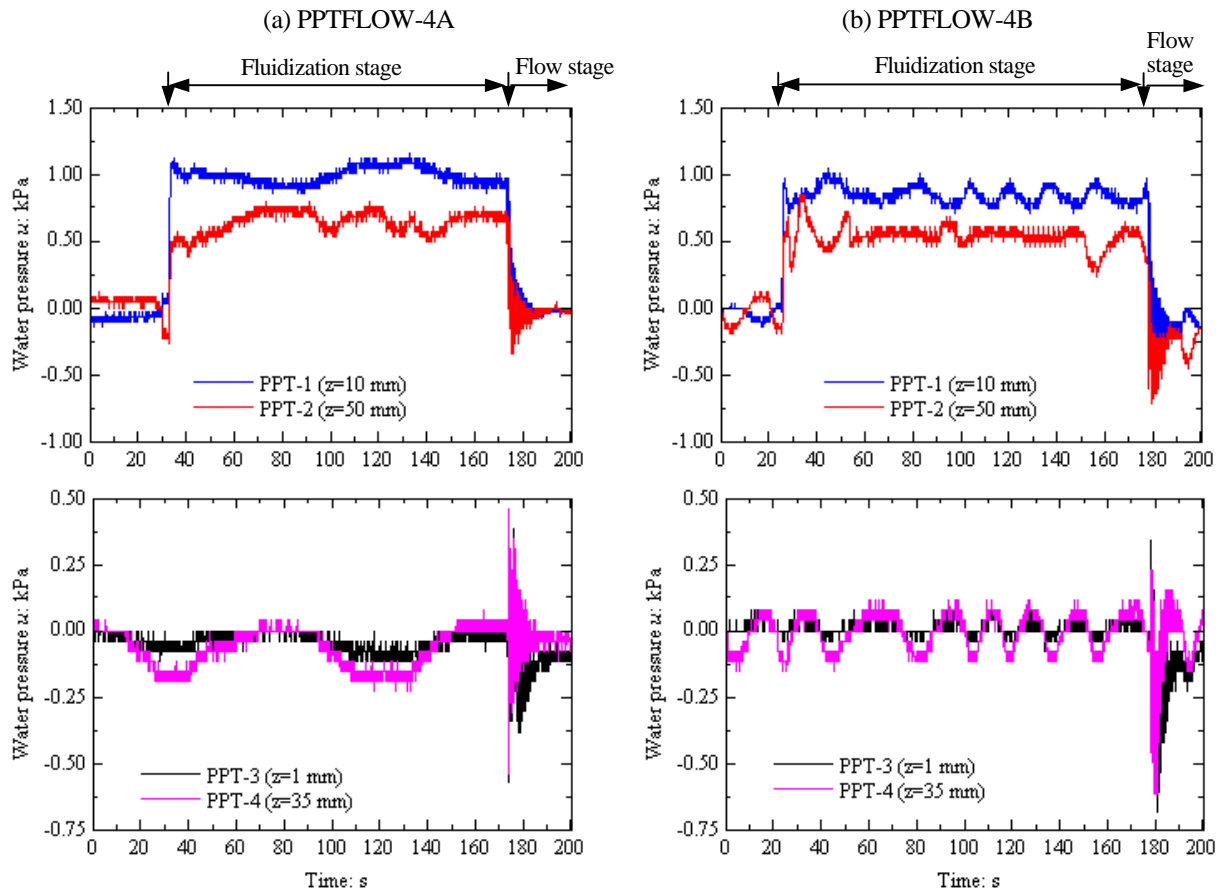
(a) PPTFLOW-4A   (b) PPTFLOW-4B

Fig. A-4 Measured time histories of water pressures in sediment gravity flow experiment (PPTFLOW-4)
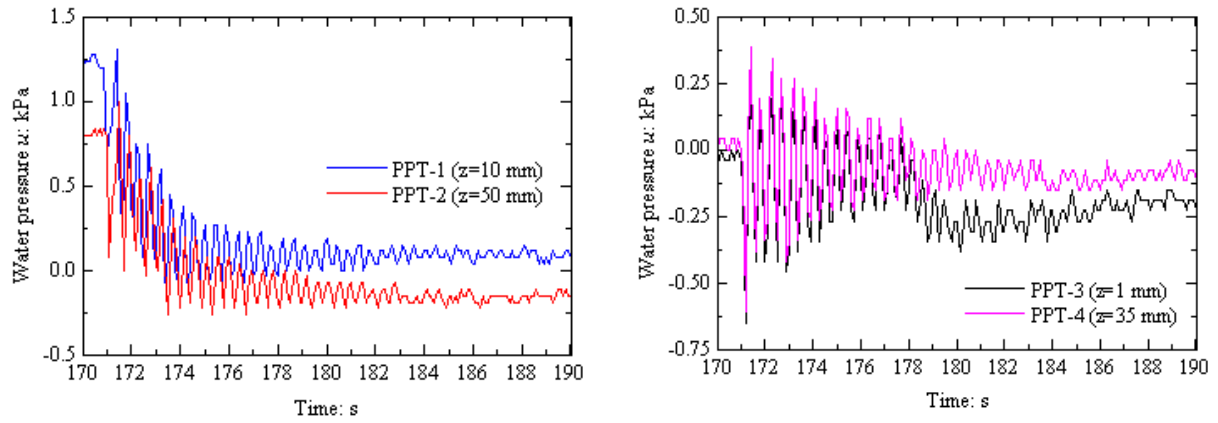
Fig. A-5 Measured time histories of water pressures after the release of the gate (PPTFLOW-1)
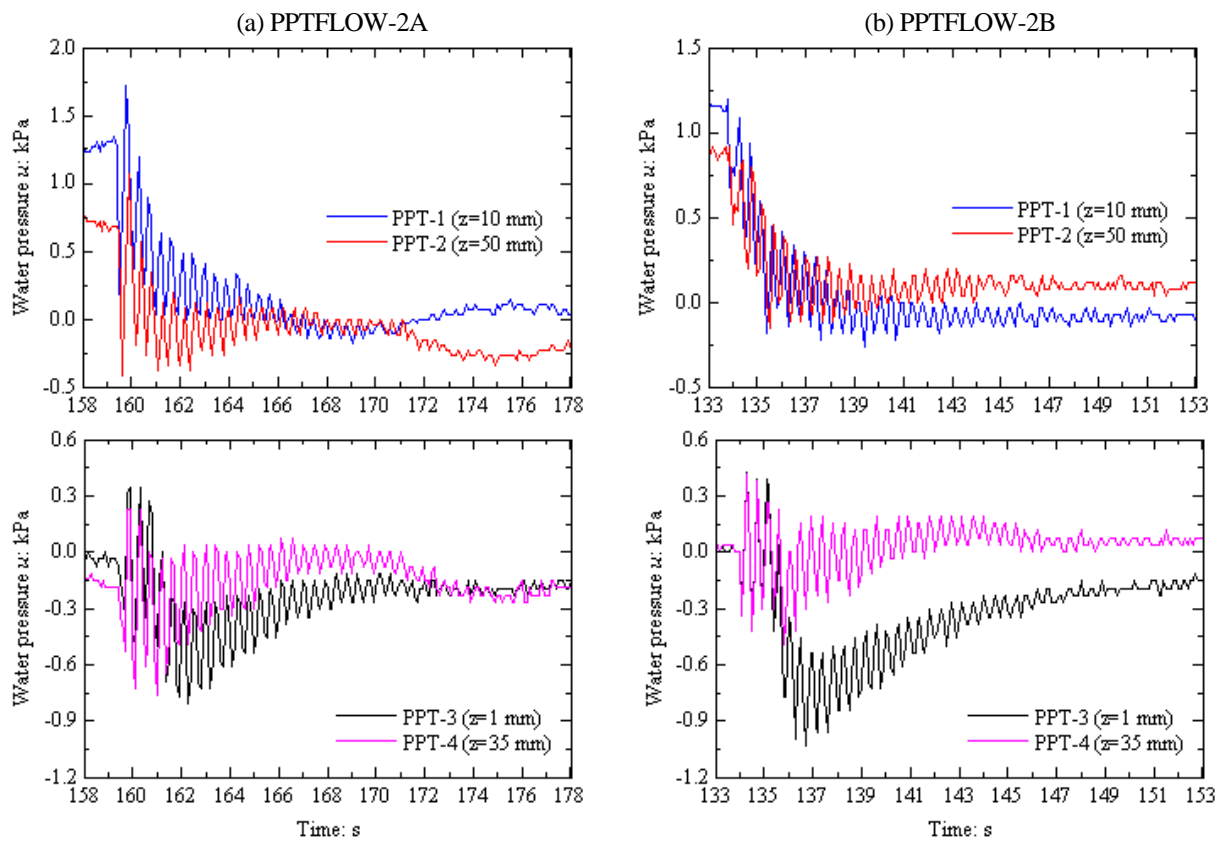
Fig. A-6 Measured time histories of water pressures after the release of the gate (PPTFLOW-2)
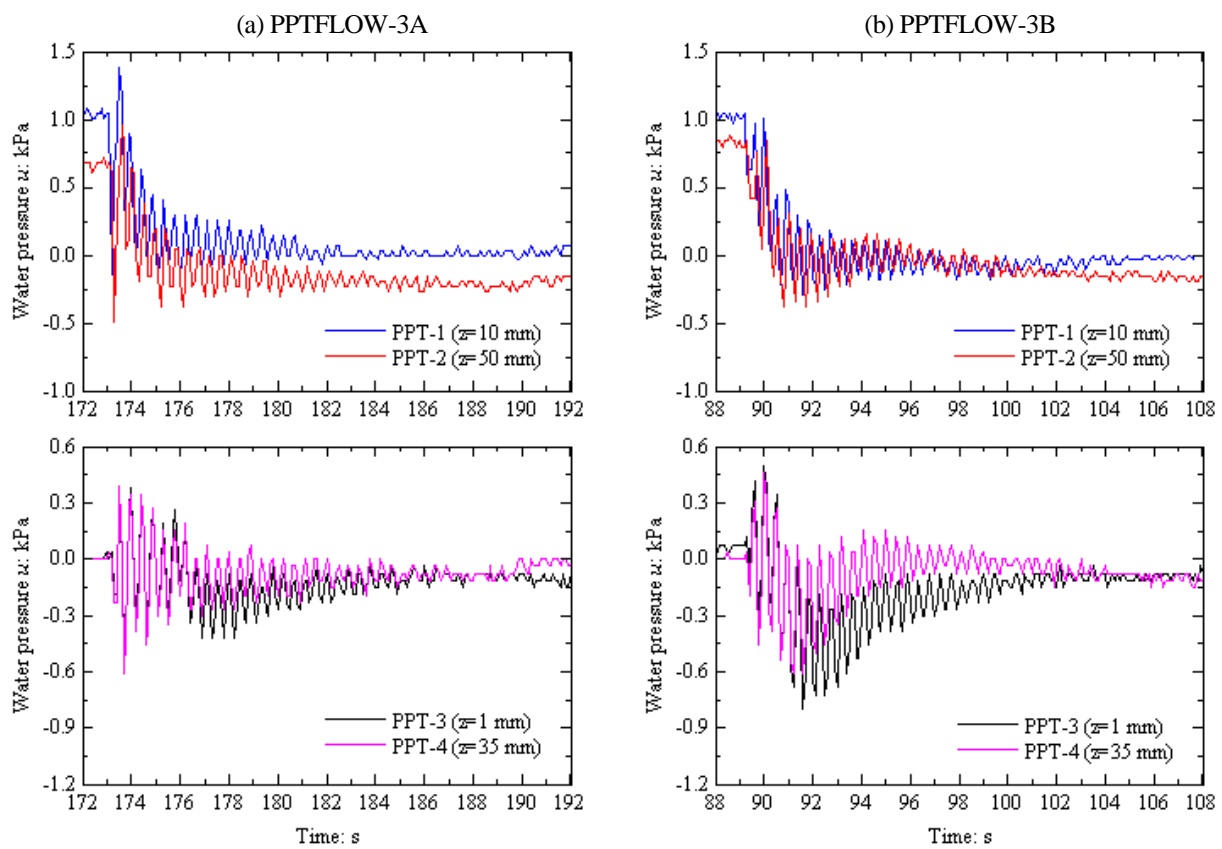

Fig. A-7 Measured time histories of water pressures after the release of the gate (PPTFLOW-3)
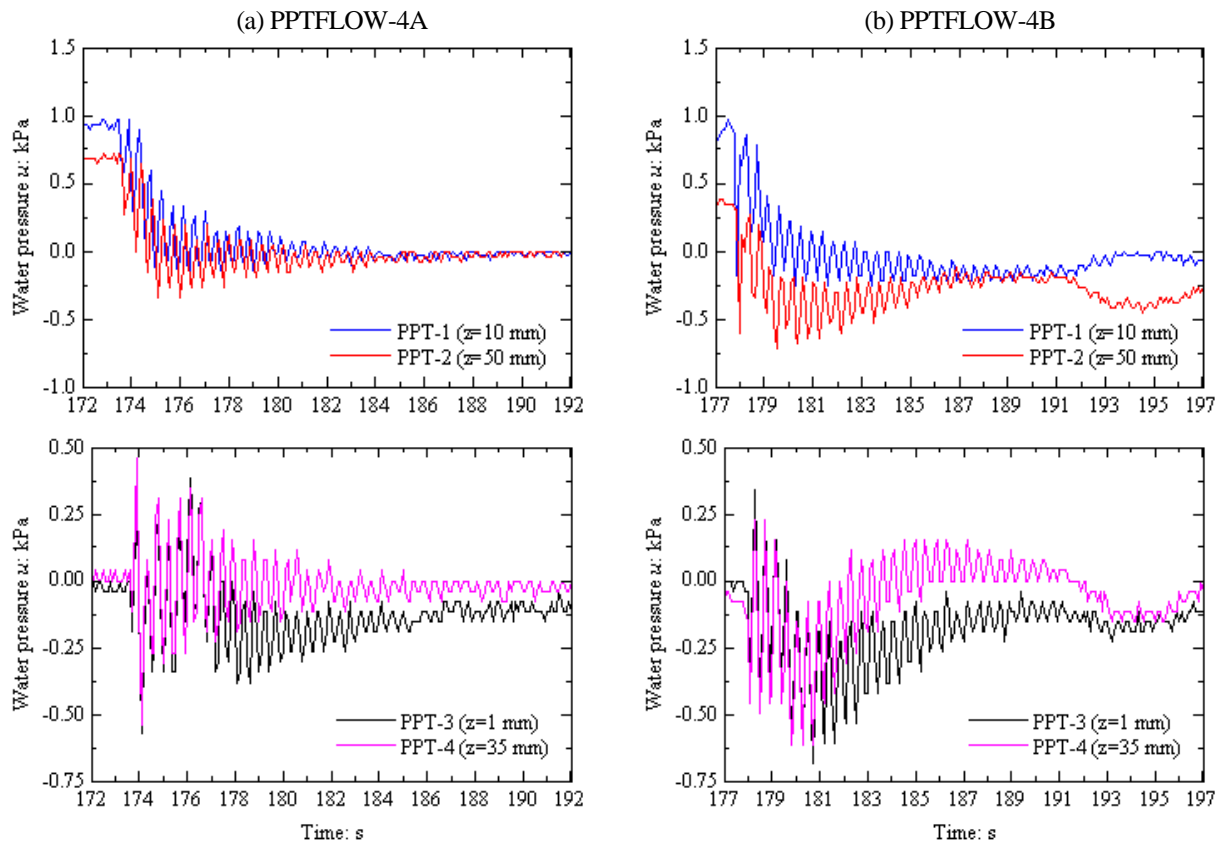
Fig. A-8 Measured time histories of water pressures after the release of the gate (PPTFLOW-4)

Amiruddin[*]   [**]

[*]

[**]   3-1-1

CCD   PIV (particle image velocimetry)